

Shape-Controlled TiO₂ Nanocrystals for Na-Ion Battery Electrodes: The Role of Different Exposed Crystal Facets on the Electrochemical Properties

Gianluca Longoni,[†] Rosita Lissette Pena Cabrera,[†] Stefano Polizzi,[‡] Massimiliano D'Arienzo,[†] Claudio Maria Mari,[†] Yi Cui,[§] and Riccardo Ruffo^{*,†,§}

[†]Dipartimento di Scienza dei Materiali, Università degli Studi di Milano Bicocca, via Cozzi 55, 20125 Milano, Italy

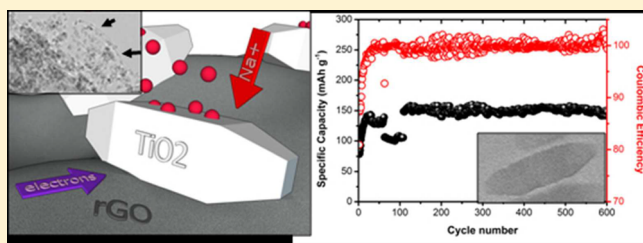
[‡]Dipartimento di Scienze Molecolari e Nanosistemi, Università Ca' Foscari Venezia and Centro di Microscopia Elettronica "G. Stevanato", Via Torino 155/b, 30172 Venezia-Mestre, Italy

[§]Materials Science and Engineering Department, Stanford University, 476 Lomita Mall, 94305 Stanford, California, United States

S Supporting Information

ABSTRACT: Rechargeable sodium-ion batteries are becoming a viable alternative to lithium-based technology in energy storage strategies, due to the wide abundance of sodium raw material. In the past decade, this has generated a boom of research interest in such systems. Notwithstanding the large number of research papers concerning sodium-ion battery electrodes, the development of a low-cost, well-performing anode material remains the largest obstacle to overcome. Although the well-known anatase, one of the allotropic forms of natural TiO₂, was recently proposed for such applications, the material generally suffers from reduced cyclability and limited power, due to kinetic drawbacks and to its poor charge transport properties. A systematic approach in the morphological tuning of the anatase nanocrystals is needed, to optimize its structural features toward the electrochemical properties and to promote the material interaction with the conductive network and the electrolyte. Aiming to face with these issues, we were able to obtain a fine tuning of the nanoparticle morphology and to expose the most favorable nanocrystal facets to the electrolyte and to the conductive wrapping agent (graphene), thus overcoming the intrinsic limits of anatase transport properties. The result is a TiO₂-based composite electrode able to deliver an outstandingly stability over cycles (150 mA h g⁻¹ for more than 600 cycles in the 1.5–0.1 V potential range) never achieved with such a low content of carbonaceous substrate (5%). Moreover, it has been demonstrated for the first time that these outstanding performances are not simply related to the overall surface area of the different morphologies but have to be directly related to the peculiar surface characteristics of the crystals.

KEYWORDS: Sodium ion batteries, energy storage, anatase, TiO₂, nanoparticle facets



Efficient energy storage will be an essential asset in a society increasingly starved of energy. If the economically and industrially developed countries stick to their current policies, the world's energy needs will be 50% higher in 2030 than today, with a suggested annual growth rate of 1.6%. Despite the pivotal role of developed countries in paving the way toward a more energetically sustainable and less fossil fuel dependent future, two-thirds of the energy demand's steady increase will derive from currently developing countries. Leading parties of the latter argue that, in a free market landscape, it is rather unfair to intervene with strict international policies regarding emission curbing and fossil fuel exploitation restraints, since this would represent a violation of the legitimate right to growth, experienced by developed countries in the past centuries. The transition toward a more sustainable development passes necessarily through a more efficient handling of energy production and exploitation, whichever the energy source might be. Energy storage, in particular, is of primary importance in many fields, such as the effective integration of

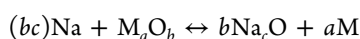
renewable energy sources (RES) and power quality and reliability.¹ Among the energy storage technologies today available, such as pumping hydro, mechanical (flywheels), electrical, chemical, and electrochemical,² secondary batteries represent the more versatile and efficient choice. Lithium ion batteries (LIB), in particular, have embodied for more than two decades the role of the highest performing electric storage facility, thanks to their high round trip efficiency, prominent energy density, and notable power density.^{3–5} The massive diffusion of lithium-ion battery technology in the last 20 years contributed to the arise of concerns connected to the future availability of battery-grade lithium compounds, especially considering energy-intensive applications of the technology, such as the electric vehicles market and on grid storage

Received: October 17, 2016

Revised: December 16, 2016

Published: December 27, 2016

facilities.^{6,7} The picture gets grimmer if all other applications that require a considerable amount of lithium are considered; indeed, battery manufacturing accounts for only 30% of the world lithium production (measured as LCE, namely, the unit of lithium carbonate equivalent), and other applications include glass, lubricant, and metallurgy industries.⁸ Lastly, is the implementation of lithium energy storage technology actually heading for a curtailment of CO₂ emissions? The steady increase of the utilization of LIB forecasted for the next few decades casts a shadow on the actual environmental friendliness of all of the phases of battery manufacturing. Life cycle assessments (taking into account battery production, materials processing, and recycling) have revealed that 400 kW h is needed to make a 1 kW h Li-ion battery, with an associated CO₂ emission of about 75 kg, equivalent to burning 35 L of gasoline.^{7,9} Owing to these considerations, other battery chemistries have begun to be investigated in the recent times. Sodium ion battery technology (SIB) has recently known a renaissance and a renovated interest thanks to the rather similar chemistry to LIB and, above all, thanks to the unique abundance of raw materials.^{10,11} Studies have revealed how switching to SIB technology would reduce production costs especially connected to materials manufacturing.¹² Materials for the SIB positive electrode have been extensively investigated: easy-to-manufacture and environmentally friendly compounds with promising features in terms of energy density and cyclability have been proposed. Layered oxides of naturally abundant transition metals,^{13,14} similar to those employed in LIBs, showed interesting electrochemical properties in intercalating Na⁺: for instance, gravimetric capacities well above 150 mA h g⁻¹ have been measured for P2-Na_{2/3}[Fe_{1/2}Mn_{1/2}]O₂.¹⁵ Following the success of phospho-olivines, introduced by Goodenough as a Co-free positive material for lithium batteries,¹⁶ a large number of polyanion compounds have been suggested as promising materials for SIB, exploiting the benign effect of [PO₄]³⁻ on working potential tailoring. Fluorophosphate (Na₂MnPO₄F¹⁷) and pyrophosphate^{18–21} have been extensively studied as well. Among the latter, a Na₂FeP₂O₇-carbon nanotube composite has been reported to achieve outstanding stability and kinetic properties.²² Despite all of these admirable efforts in designing a robust positive cathode, the most demanding challenge is represented by the negative electrode. Many exhaustive reviews have been published providing an in-depth description of the anode materials proposed along the years.^{12,23–25} Fundamental prerequisites for SIB anode materials are (i) a high capacity and low operational potential, (ii) chemical stability and high Coulombic efficiency, and (iii) a natural abundance of precursors and scalable synthetic routes. Concerning the accessibility of synthetic routes and scalability of processes, transition metal oxides represent a valid choice. Fe₃O₄^{26,27} and Co₃O₄^{28,29} have been reported as valuable anode material compounds for SIBs thanks to their easy preparation and high theoretical capacity (~890 mA h g⁻¹). The courageous proposition of this kind of materials signs a complete paradigm shift in the chemistry involved in alkaline metal-based batteries. The classic rocking chair intercalation mechanism (core process in the graphite-lithium metal oxide battery) is abandoned in favor of compounds that interact with sodium via the conversion reaction:²⁴



where M_aO_b is a general transition metal oxide. The reported reaction relies just on an ideal behavior, while the actual mechanism might include products other than Na₂O (thermodynamically stable in most cases) and the bare metal M. For instance, Su et al.³⁰ claimed that CoO is involved in the reversible (de)lithiation of a Co₃O₄ anode rather than Co₃O₄ itself, which has been demonstrated to undergo an irreversible transformation during the first lithiation cycle. A well agreed-upon flaw of this class of materials is the intrinsic poor cyclability, due to excessive volume change experienced during conversion reactions. The relevant stresses the active material particles are exposed to, led to the sudden fracturing of particles and rupturing of the SEI (solid electrolyte interface) layer and drive the whole system toward a gradual deterioration of capacity retention. A transition metal oxide that seems to answer to this technological challenge is TiO₂. TiO₂ polymorphs have been extensively investigated as potential anode materials for SIBs thanks to their exceptional stability, nontoxicity, natural abundance, and low cost. Despite being chemically active toward Li intercalation, anatase-TiO₂ does not intercalate efficiently Na ions. Even though anatase polymorphs present the least dense packing of TiO₆ octahedra, Na⁺ ion dimensions appear to be a limiting factor for reversible insertion in the lattice. Nevertheless, anatase-TiO₂ has been demonstrated to give a decent capacity of 180 mA h g⁻¹ at 0.2 C and a considerable stability over cycles.³¹ Recent studies by Passerini on commercial anatase powders unveiled different mechanisms contributing to the total capacity of TiO₂ in SIB.³² In particular, after a pseudocapacitance behavior, accounting for 4% of the total capacity extracted during the first cycle (360 mA h g⁻¹), a considerable amount of charge is stored via what it has been demonstrated to be, an insertion process of Na⁺ in TiO₂ lattice which occurs at intermediate potentials (1.0–0.3 V vs Na/Na⁺). Below 0.3 V, a significative and progressive deterioration of the crystallinity of the material, not recovered in the following cycles, takes place. Despite the multiplicity of anatase structures and morphologies analyzed so far, data relative to capacities and, most of all, stability of the compound through cycling are still scattered and controversial.^{33–36}

In this work we tried to shed light onto the general mechanism underneath the interaction between sodium ions and different TiO₂ morphologies, giving particular attention to how different exposed crystal facet ratios might influence and guide the intercalation and conversion mechanisms. Inspired by the exploratory work by Dihn et al.³⁷ and following outstanding contributions to materials synthesis,^{38,39} we have been able to selectively obtain anatase-TiO₂ nanocrystals with three peculiar surface characteristics by solvothermal route employing tetrabutyl orthotitanate (TB) as a TiO₂ precursor and in the presence of capping agents (oleic acid and oleylamine). Relative ratios of oleic acid and oleylamine (OA:OM, see details in the SI) and reaction temperature have been accordingly modulated in order to express the growth of different crystalline facets. A thorough decapping phase using an oxidizing compound (nytrosil tetrafluoroborate) has been chosen in order to prepare clean TiO₂ samples utilized as reference materials. This phase has also served as a preparatory step for a further functionalization of TiO₂ crystal surfaces by (3-aminopropyl)-triethoxysilane (APTES). Aminic terminations of APTES molecules grafted onto TiO₂ crystals have been eventually utilized to induce a 5% by weight graphene oxide (GO), synthesized using a modified Hummer's method⁴⁰) wrapping, exploited to improve the electronic conductivity of the material.

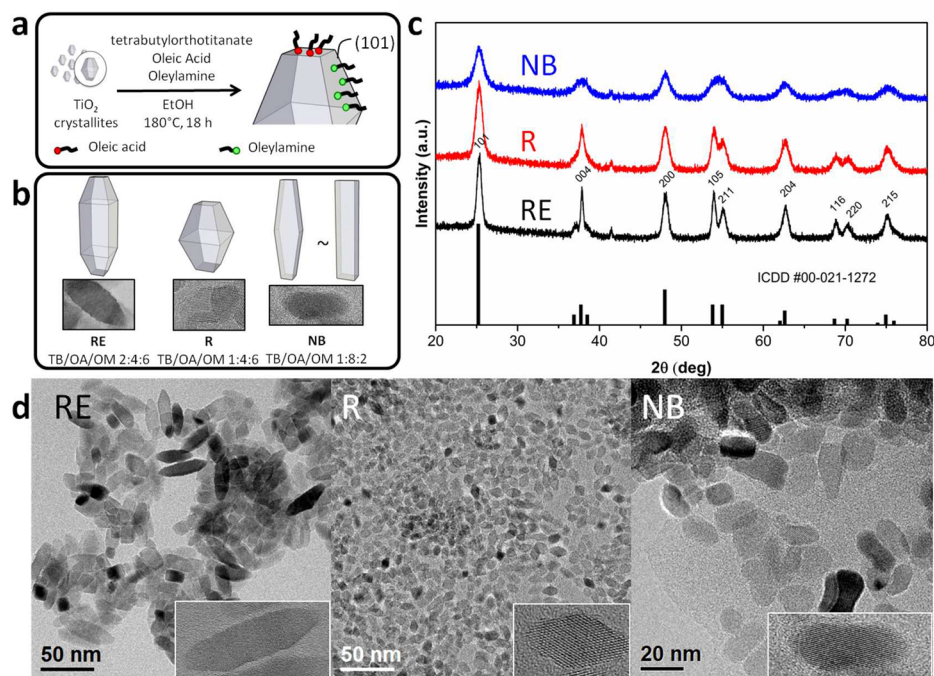


Figure 1. (a) Schematic representation of the shape-controlled growth mechanism and synthesis condition of TiO_2 crystallites thanks to the selective capping effect of oleic acid (OA) and oleylamine (OM); (b) 3D sketch of the investigated morphologies with the corresponding TEM magnification on single particles and the relative amount of the three reactants employed in the synthetic routes; (c) X-ray diffractograms of anatase- TiO_2 nanocrystals (RE black, R red, and NB blue lines) and PDF card 00-021-1272 peaks of tetragonal anatase (vertical black lines); (d) TEM images of the as-synthesized anatase- TiO_2 morphologies. In the inset of each figure, the HRTEM image of a single particle is shown.

Graphene oxide impregnation of functionalized TiO_2 crystals has been carried out in aqueous media by dropping a graphene oxide stable water suspension. The final composite has been subsequently subjected to a heat treatment in an inert atmosphere to achieve a partial reduction of GO to reduced graphene oxide (rGO). An accurate morphological and electrochemical characterization has been subsequently performed to clarify the sodium uptake mechanisms occurring in a Na-ion half cell battery using the nanostructured composite as an active anode material.

The TEM images of the three pristine powders (without GO) after the decapping process are reported in Figure 1d: all of the structures appear highly uniform in shape and in particle dimensions. According to the reaction mechanism sketched in Figure 1a, selective adsorption of oleic acid (OA) occurs onto high energy crystalline facets (001), while oleylamine (OM) molecules are adsorbed preferentially onto lower energy (101).^{38,39} Owing to these considerations, the modulation of the TB:OA:OM ratio allows the crystal growth along specific directions. Moreover, the concentration of titanium precursor plays a key role in determining the final morphology. In detail, for OA:OM ratio = 4:6, an increase of Ti concentration leads to the particle elongation along the [001] direction, resulting in an elongated rhombohedral morphology (RE) (Figure 1d). Keeping constant the relative amount of OA and OM but sensibly decreasing the TiO_2 precursor, small rhombic crystals (R), outstandingly homogeneous in shape and dimensions, have been obtained (Figure 1d). On the other hand, a large excess of oleic acid sensibly limits the particles growth, due to the strong adsorption of the carboxylic acid also onto crystalline facets other than (001),³⁸ and produces slightly smaller crystals that resemble parallelepipeds (i.e., nanobars, NB) in shape (Figure 1d). After the successful removal of the capping agents,

no significant agglomeration nor a preferential orientation of particles driven by high energy face to face interactions can be spotted in TEM images. XRD diffractograms reported in Figure 1c clearly support the high crystallinity of the samples as well as the absence of interfering impurities, while from the diffraction peaks width a quantitative insight on crystal dimensions, using Scherrer's relation, can be achieved. In agreement with the TEM images, the largest particles belong to the RE sample, due to the strong elongation along [001] and the high amount of TB precursor employed in the synthesis. Switching to rhombic (R) and consequently to nanobars (NB) morphology, a progressive reduction in particle dimension occurs, as can be seen also from the broadening of the X-ray diffraction peaks. Exploiting Scherrer's relation, lengths along specific crystalline directions can be calculated (and values are reported in Table S1); nonetheless due to cumulative effects contributing to XRD peak broadening, such as instrumental factors, dimensions directly measured from TEM images have been taken into consideration for further calculations. The crystal dimensions directly measured from TEM images according to criteria listed in Table S2 have been thus collected in Table 1. RE particles shows the highest anisotropy with a length (measured along [001] direction) extending up to 40 nm and a width accounting

Table 1. BET Surface Area and Crystal Dimensions Measured Manually from TEM Images along Two Crystalline Direction Corresponding to the Length and Width of Each Geometry

	[004] L_{TEM} (nm)	[200] L_{TEM} (nm)	BET surface area ($\text{m}^2 \text{g}^{-1}$)
RE	41.2	13.6	89.4
R	18.4	10.4	103.6
NB	21.3	10.8	122.3

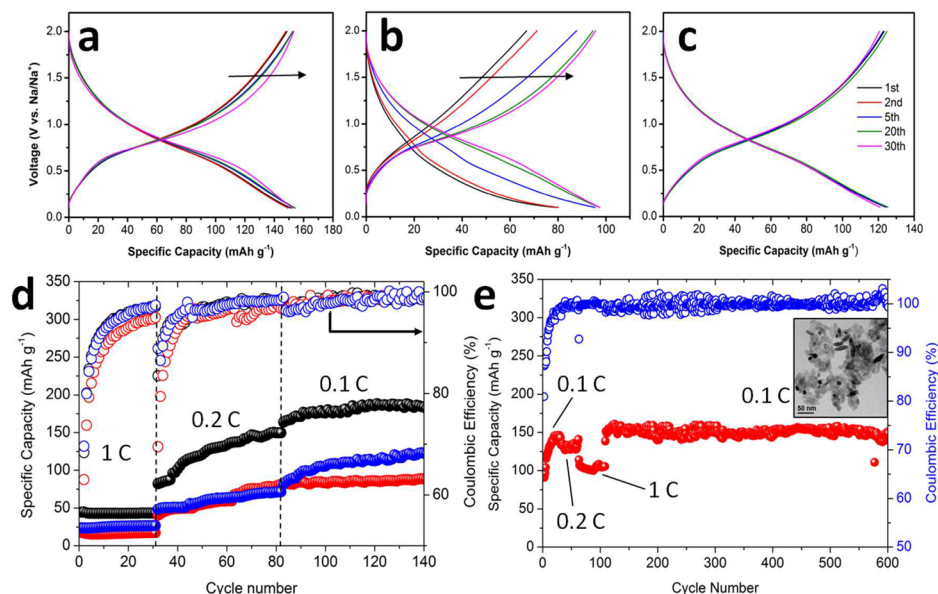


Figure 2. Charge/discharge potential profiles of RE (a), R (b), and NB (c) registered at 0.1 C (50 mA g^{-1}) after 5 preconditioning cycles at 1 C (500 mA g^{-1}). (d) GCPL performance of RE, R, and NB electrodes (black, red, and blue curves, respectively) at different C-rates. (e) Stability test performed on the RE electrode alone, over 600 cycles. In all of the electrochemical tests, cut-off potentials of 0.1 and 2.0 V vs Na/Na⁺ were used during the sodiation and desodiation steps, respectively.

for 13 nm. Conversely R and NB show comparable dimensions, measuring ca. 20 nm in length and 10 nm in width. TGA analysis of pristine TiO₂ were carried out (SI, Figure S2) before and after the cleaning treatment to measure the residual amount of organic species still adsorbed onto TiO₂ surfaces. The NB sample showed the highest weight loss (−17.7% before cleaning and −5.97% after cleaning), probably due to either the large excess of oleic acid used in the synthesis either the resulting decomposition of residual organic capping agents, which is less effectively removed from NB crystal surfaces even after a remarkable oxidative treatment. Conversely, RE and R strongly benefit from the cleaning procedure, since only weight losses of 0.32% and 1.19%, respectively, are observed. The water content, adsorbed on crystal surfaces and causing the sample weight loss below 200 °C, is limited to few percentage points (<5%) for all of the morphologies.

The actual exposure of the hypothesized crystalline facets has been confirmed also from HRTEM images (SI, Figure S3a–f). The RE crystals revealed the {101} and {002} exposed facets. The distance referred to {200} planes can be measured along the direction perpendicular to the middle rectangular section of RE particles ($d_{200} = 0.37 \text{ nm}$). This is a proof that, unlike R crystals, RE exhibits also {200} and {010} facets exposed. In the case of NB particles, only {101} and {011} facets, and the corresponding plane spacing (0.35 and 0.34 nm, respectively), can be clearly distinguished. In NB {101} are believed to be less prominent relatively to {001}, if compared to the R and RE case. Angles between detectable crystalline planes have been also measured, since their amplitude is a further confirmation of the presence of specific lattice planes. The angle spanning between the supposed {001} and {101} planes shows an amplitude of 68.9°, close to the theoretical one (68.3°). The evaluation of the percentage exposure of crystalline, essential to elucidate the correlation between electrochemical performances and crystal characteristics, has been done using relatively simple geometric equations conveniently modified to fit different crystal shapes and collected in the SI.

The relative percentage of surfaces has been summarized in Figure S3g, in the SI, in which also the energetic content of each surface is intuitively sketched thanks to the color palette, assigning the green color to the less energetic one, namely, {101} with 0.44 J m^{-2} surface energy density, and the red color to {001} facets with the highest value of surface energy density (0.90 J m^{-2}) according to literature.³⁹ It is worth noticing how the relative ratio between {101} and {001} exposure is kept constant (about 19:1) for RE and R. This can be connected to the relative amount of OA and OM used, which was the same for the two morphologies, and which directed {001} and {101} growth in similar fashion. This ratio decreases significantly (4:1) in the case of NB, in which the contribution of {001} to the total surface of the particles is higher. Growth along [001] direction has been indeed hindered due to the relevant absorption of oleic acid on {001}, driving crystal development along other crystalline directions. To confirm the successful graphene oxide wrapping of anatase particles, TEM images have been taken after the wrapping procedure (SI, Figure S3h,i). Graphene sheets, probably made of the stacking of multiple single graphene layers, can be easily spotted and are highlighted in the pictures with red arrows pointing at their edges. As it can be furthermore noted, TiO₂ crystals have preserved their morphologies despite the thermal treatment, without undergoing significant agglomeration, Ostwald ripening process, or oriented attachment by specific surfaces as suggested in literature,⁴¹ and appearing securely grafted onto the graphene oxide sheets. Presumably, it has been the effective hooking itself deriving from APTES functionalization that kept the particles away from large agglomeration phenomena.

Galvanostatic tests, for the three materials investigated, are reported in Figure 2d. The sequence of the currents used (C-rate) has been chosen accordingly to the positive effect experimented using a growing trend versus a decreasing one. In the former case, the typical activation time required to achieve a stable capacity at lower currents is strongly reduced as can be seen from cycles performed at 1 C (500 mA g^{-1}). Interestingly,

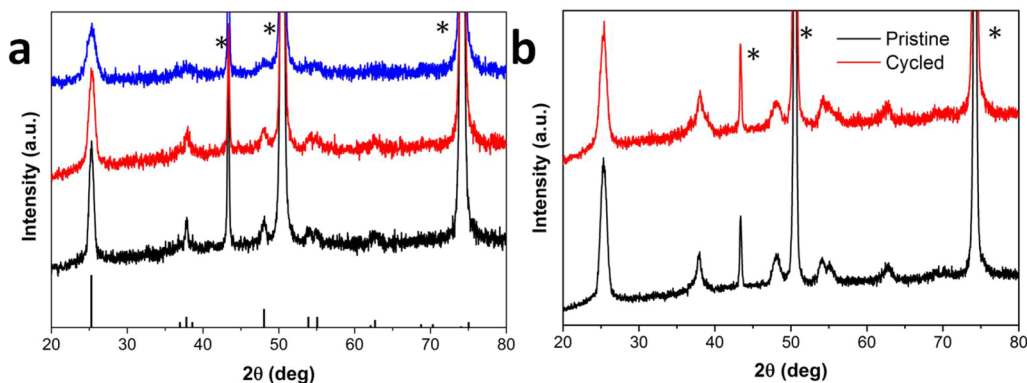


Figure 3. (a) XRD diffractograms of the RE, R, and NB electrodes (black, red, and blue line, respectively), asterisks mark the peaks coming from Cu current collector; (b) XRD diffractograms taken on a fresh RE electrode (black line) and on a cycled one (red line), after the 10th cycle of a GCPL analysis, where the last current step was a desodiation one; asterisks refer to the diffraction peaks of the Cu current collector.

all of the morphologies investigated electrochemically show increasing or steady capacities. The RE sample appeared to be the one that allowed reaching the highest capacity values at all of the three C-rates investigated. Indeed, a remarkable steady capacity of 180 mA h g^{-1} is achieved at 0.1 C after 70 cycles; for NB and R this value is limited to 123 and 88 mA h g^{-1} , respectively. An interesting aspect is that none of the three morphologies shows a gradual decline toward lower capacities, as reported in recent works investigating this material,^{36,42} this behavior represents a puzzling aspect about oxide-based anode materials for SIBs. With the increase in the cycling current to 0.2 C (100 mA g^{-1}), an almost negligible reduction in capacity is obtained. A considerable drop in capacity is instead registered for currents as high as 1 C (500 mA g^{-1}): only 45 mA h g^{-1} can be extracted from rhombic elongated crystals (RE), and even a lower amount, 26 and 16 mA h g^{-1} , from NB and R morphologies, respectively. Some may argue that the not so impressive rate capabilities of the prepared materials might be a severe limit, but we believe that a noteworthy improvement is possible by optimizing the graphene oxide wrapping procedure of TiO_2 nanoparticles. As illustrated by TEM images (SI, Figure S5), the condition under which the graphene oxide wrapping is obtained namely the not optimal fragmentation of TiO_2 agglomerates when TiO_2 is suspended in water, leads to TiO_2 conglomerates wrapping to be achieved, instead of single particles grafting on graphene sheets. The core of these isolated pomegranate-like structures is less available for electrochemical processes, and the insulating nature of anatase- TiO_2 makes this effect even worse at higher current rates. Nevertheless the stability of the material over cycles is remarkable, and as can be seen from the cycles performed at 1 C (500 mA g^{-1}) in Figure 2e, a capacity of 105 mAh g^{-1} can still be obtained. To better elucidate the motivation beyond the mild concentration of rGO employed, compared to other works in which higher content (10 wt %) is utilized,⁴³ a comparison between the electrochemical properties of RE, R, and NB nanocrystals with and without the reduced graphene oxide wrapping, has been provided (SI Figure S3). The results have been reported in terms of specific capacities normalized over the specific BET area of the samples (see Table 1), obtaining a parameter expressed in mA h m^{-2} of active material, plotted against the cycles number. This allowed us to highlight that the pure surface contact with the surroundings, namely, the specific surface area of the sample, heavily affects the electrochemical performances without the beneficial effect of an electronically

connecting substrate capable of overcoming the conductive limits of TiO_2 nanocrystals. Presumably the major reactivity deriving from crystalline facets with high surface energies {001} plays role in driving sodium uptake. As a matter of fact, in the capacity density graphs of pristine TiO_2 , the NB sample, provided with the higher percentage of high energy surfaces, shows comparable performances to RE and R (SI, Figure S4a) despite its high surface area. Nevertheless, the higher energetic profile of NB is also accountable, as reported in literature,⁴³ for a selective interaction with GO, this leads to the blockage of {001} facets and to the consequent severe limitation in capacity density. The case of RE morphology, instead, stresses the importance of having intermediate energy density facets available. It can be indeed assumed that low percentage of {001} of RE guides TiO_2 -GO interactions as well, but instead of witnessing a deterioration of electrochemical performances, a considerable amount of capacity density is gained, together with an improvement in performances at higher currents of the material (SI, Figure S4b). It is then believed that 5% by weight graphene wrapping embodies a sensible trade-off, behaving as an efficient electron conductive substrate without heavily interfering with surface properties of the material. rGO wrapped crystals illustrates how a great difference between RE, R, and NB capacity densities is achieved (SI, Figure S3b). Coulombic efficiencies give an important insight into the reversibility of electrochemical processes. They hover around 99% for rGO wrapped RE, R, and NB as well, which is a symptom of the electrochemical processes reversibility as well as the stability of the formed SEI layer. An outstanding average Coulombic efficiency value of 99.55% is achieved over more than 500 cycle in the case of RE. An overall stability of the morphological and structural properties of the active material is thus suggested. Lower values of the Coulombic efficiencies are often indicative of a recursive SEI formation mechanism, occurring during each sodiation step; this is ascribed to severe volume changes of material particles that produces the detachment and fracturing of the present SEI layer. Potential profiles, as illustrated in Figure 2a–c, resemble those of extremely reversible processes. Operative potentials, similar for RE, R, and NB, are as low as 0.83 V vs Na/Na⁺, and represent an interesting starting point for the implementation of these materials as low-cost anodes for SIBs. This value is sensibly lower than that referred to Li intercalation in lithium titanates⁴⁴ ($\sim 1.8 \text{ V vs Li/Li}^+$), an aspect that makes TiO_2 anodes in SIBs notably more interesting for practical applications.

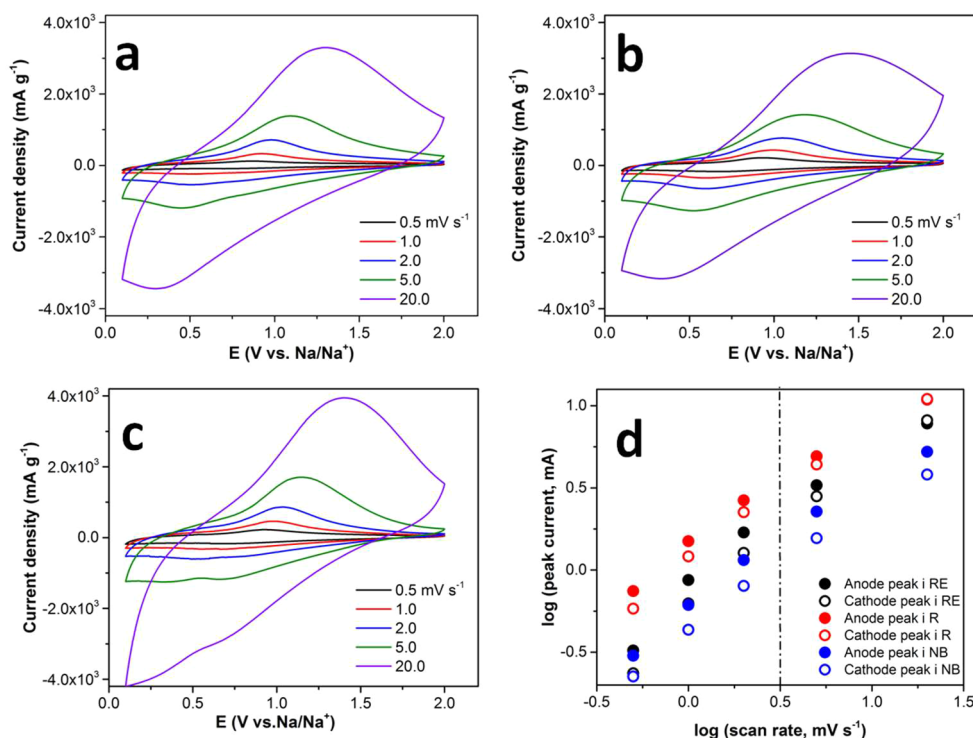


Figure 4. (a) E, (b) R, and (c) NB cyclic voltammetry curves of pure samples (no GO wrapping) registered at different scan rates; (d) $\log(i)$ – $\log(v)$ plot for the investigated morphologies where the vertical dashed line separates the linear regime (b -value = 1) from the nonlinear one (b -value < 1) of $\log(i)$.

A considerably longer activation process is required for R (Figure 2b): only after the 30th cycle a steady capacity close to 100 mA h g⁻¹ can be achieved. On the other hand, RE and NB reach a stable regime much sooner, and in the case of RE even a slight decrease in the sloping character is obtained. Contrary to what is reported in literature about the particle size and electrochemical behavior of anatase TiO₂, we observed that a higher size, and particularly a higher aspect ratio, is beneficial to the electrochemical performance of the material. This is here attributed to the different morphological features of the nanoparticles. In the works of Passerini⁴⁵ and Mulder et al.,⁴⁶ averagely spherical particles, with no predominance in crystalline facets exposure, were taken into consideration. Considering these systems, what might be a peculiar effect of Na interaction with crystalline surface is dampened, and the only significant factor heavily limiting the electrochemical behavior, as capacity and rate capabilities, is the better electronic conduction achieved with smaller TiO₂ particles, in the nanometric range, compared to larger ones. A direct confirm of the retained anatase phase and size properties during the galvanostatic cycling was given by ex situ XRD analysis taken on a cycled RE electrode (Figure 3b). After 10 cycles at 0.1 C, not only the anatase phase is preserved, without the appearance of any notable impurity, but also the dimensions computable from peaks full widths at half-maximum are comparable with those of the pristine material. For completeness, also the X-ray diffractograms for each electrode material have been reported in Figure 3a.

The electrochemical reaction mechanism of sodium ions with anatase TiO₂ has been the subject of several investigations. Different mechanisms, depending on the charge state, particle sizes and shape have been proposed and validated. Indeed, submicrometric particles have shown a state of charge-

dependent behavior with three different regimes: a pseudocapacitive region at high potential (short capacity), the structural intercalation in the particle bulk (up to 0.7 Na per unit formula), and a further conversion reaction at low potential.³² However, it has been also demonstrated that, when using much smaller particles or nanostructures, the pseudocapacitive domain is extended and the pseudocapacitive capacity becomes dominant;³³ indeed, intercalation pseudocapacitance has been already found to be the prevalent capacitance harvesting mechanism in a 10 wt % graphene-TiO₂ compound, due to the Na⁺ fast intercalation in gaps formed between TiO₂ surfaces and partially bonded graphene sheets.⁴³ To elucidate the nature of the capacity extracted from our TiO₂ nanocrystals, cyclic voltammetry tests were performed on pure RE-TiO₂ electrodes (without graphene oxide wrapping). We found out that also for naked TiO₂ nanocrystals an intercalation pseudocapacitance behavior can be highlighted: from the $\log(i)$ – $\log(v)$ plot (Figure 4d), current values collected from CV peaks at different scan rates (0.5, 1, 2, 5, 20 mV s⁻¹) correlate linearly to the scan rates for values lower or equal than 2 mV s⁻¹ (Figure 4d), while they slightly deviate from the linear relation above this value. This hints for a progressive shift from a capacitive behavior toward a diffusion-controlled electrochemical process, with an increase in the scan rate. Mathematically this coincides with a change in b -value, calculated from the slope of the $\log(i)$ – $\log(v)$ curve, from 1 to 0.8, in the following equation:

$$i = av^b$$

where v is the scan rate used in the measurement. For this reason, since the peak currents do not scale with $v^{1/2}$, the capacity must originate from a capacitive-like mechanism. This feature together with the slight shifts in peak potentials at low

scan rates support the hypothesis of a bulk intercalation capacitance as it has been highlighted for other oxides such as Nb_2O_5 .⁴⁷ It can be also argued that a percentage of the observed capacity might be also related to a pure double-layer capacitive mechanism. Typically, the amount of capacity coming from this type of non-Faradaic process in nonaqueous electrolyte lies between 10 and 50 $\mu\text{F cm}^{-2}$, while pseudocapacitive behaviors, including intercalation pseudocapacitance, underpin values by 10–1000 times higher.⁴⁸ From cyclic voltammetry curve integration of a non-Faradaic portion of potential sweep and application of well-known equations reported in literature,⁴⁹ an esteem of the capacity density can be made for RE. The calculated value sets 26 $\mu\text{F cm}^{-2}$, which perfectly agrees with the esteemed values for pure double-layer capacitive behavior. Concerning the occurring Faradaic processes, they accurately resemble the intercalation pseudocapacitive voltammetric signals already highlighted for Li in TiO_2 polymorphs,^{50,51} namely, broad peaks with slight drifts at high scan rates, and with peak currents progressively proportional to scan rate.

In summary, three different nanostructured TiO_2 morphologies have been successfully synthesized using a solvothermal method implying surfactants as capping agents to direct TiO_2 crystal growth. Rhombic elongated (RE), rhombic (R), and nanobar (NB)-like particles clearly show noticeable differences in crystal face type exposition, as well as a substantial different behavior for what concern the interaction with sodium ions inside a Na-ion half cell. Introducing 5% of reduced graphene oxide into the samples, we can effectively study and direct the attention to the crystalline facets exposure excluding the electrochemically limiting factors deriving from total surface area and particle size. After a deep electrochemical investigation, we can conclude that an overcoordinated state of Ti atoms on the crystal surface (low energy density (101) facets of NB and R moieties) strongly inhibits the sodium uptake, while a Goldilocks condition seems to occur for crystalline faces with intermediate energy densities, like (100) in RE. These experimental results are also backed up by recent theoretical studies performed on conveniently cleaved TiO_2 anatase crystals. Yang stressed the importance of the energy state of the crystal surface in promoting sodium attachment, the surfaces themselves being the gateways for the sodium atom from the electrolyte into the lattice.³¹ The attachment energies are identified by the equation reported below:

$$E_{\text{at}} = -(E_{\text{Na-hkl}} - E_{\text{hkl}} - E_{\text{Na}})/n$$

Here E_{hkl} and $E_{\text{Na-hkl}}$ are total energies of the crystalline surfaces before and after sodium atoms attachment onto a specific $\{hkl\}$ surface. E_{Na} is the energy of sodium atoms, and n is the number of sodium atoms linked to the surface per unit area. E_{at} values have been calculated for (100), (001), and (101) to be 1.51, 0.33, and 0.50 eV, respectively.^{52,53} As can be noted, this trend is in contrast with the one expressed by TiO_2 surface energies alone (SI, Figure S3), from which the (001) facets appeared to have the higher reactivity. The reason why this order is twisted must be sought in the n parameter, specific for each face and dependent on available sites for sodium attachment. This parameter is higher for the (001) facets, due to a higher concentration of oxygen octahedrons on it, and thus the resulting E_{at} per sodium atom per unit area ends up to be the lower among those considered. The surpassingly favored energetic interaction with (100) facets must be furthermore attributed to a better accommodation of Na atoms on the

monatomic step on the facet, while the (001) planar surface forces sodium atoms to pack with a higher density and thus conveying lateral unfavorable interactions. For what concern Na uptake mechanism, the change from a linear to a polynomial dependence between peak currents and scan rate, in a double logarithmic plot, clearly evidence an intercalation pseudocapacitance contribution to the total material capacity, at least for what concerns moderate current densities. The reduced graphene oxide– TiO_2 composite, allows to obtain outstandingly stable capacities ($\sim 150 \text{ mA h g}^{-1}$ for more than 600 cycles) never achieved with such a low content of carbonaceous substrate (5 wt %), in literature at best of our knowledge. It has been also proven that these notable performances are not related to the overall surface area of the different morphologies but have to be directly connected to the peculiar surface characteristics of the crystals. Further efforts have to be directed in overcoming the puzzling irreversible capacity connected to the first cycle, particularly evident if low current are used. Owing this, we believe that in the future design of oxide-based and TiO_2 -based anode materials for SIBs special consideration must be addressed to the crystalline characteristics of the particles and to theoretical studies concerning the Na interaction with surfaces with a different energetic content.

■ ASSOCIATED CONTENT

Supporting Information

The Supporting Information is available free of charge on the ACS Publications website at DOI: 10.1021/acs.nanolett.6b04347.

Additional data containing synthetic route details, ancillary structural characterization, and electrochemical performances helpful to an in-depth understanding of the investigated subject (PDF)

■ AUTHOR INFORMATION

Corresponding Author

*E-mail: riccardo.ruffo@unimib.it.

ORCID

Riccardo Ruffo: 0000-0001-7509-7052

Notes

The authors declare no competing financial interest.

■ REFERENCES

- (1) Electrical Energy Storage Technology Options. *Electr. Power Res. Inst.* 2010, Report 102.
- (2) Dunn, B.; Kamath, H.; Tarascon, J.-M. Electrical Energy Storage for the Grid: A Battery of Choices. *Science (Washington, DC, U. S.)* **2011**, 334 (6058), 928–935.
- (3) Bruce, P. G.; Scrosati, B.; Tarascon, J.-M. Nanomaterials for Rechargeable Lithium Batteries. *Angew. Chem., Int. Ed.* **2008**, 47, 2930–2946.
- (4) Goodenough, J. B. Electrochemical Energy Storage in a Sustainable Modern Society. *Energy Environ. Sci.* **2014**, 7 (1), 14–18.
- (5) Ellis, B. L.; Lee, K. T.; Nazar, L. F. Positive Electrode Materials for Li-Ion and Li-Batteries. *Chem. Mater.* **2010**, 22, 691–714.
- (6) Tarascon, J.-M. Is Lithium the New Gold? *Nat. Chem.* **2010**, 2 (6), 510.
- (7) Larcher, D.; Tarascon, J.-M. Towards Greener and More Sustainable Batteries for Electrical Energy Storage. *Nat. Chem.* **2014**, 7 (1), 19–29.
- (8) The lithium market. <http://www.signumbox.com/lithium-reports/>.

- (9) Sullivan, J. L.; Gaines, L. A Review of Battery Life-Cycle Analysis: State of Knowledge and Critical Needs. *Transp. Res.* **2010**, *45*.
- (10) Wang, L. P.; Yu, L.; Wang, X.; Srinivasan, M.; Xu, Z. J. Recent Developments of Electrode Materials for Sodium Ion Batteries. *J. Mater. Chem. A* **2015**, *3*, 9353.
- (11) Kubota, K.; Komaba, S. Review—Practical Issues and Future Perspective for Na-Ion Batteries. *J. Electrochem. Soc.* **2015**, *162* (14), A2538–A2550.
- (12) Kim, Y.; Ha, K.-H.; Oh, S. M.; Lee, K. T. High-Capacity Anode Materials for Sodium-Ion Batteries. *Chem. - Eur. J.* **2014**, *20* (38), 11980–11992.
- (13) Ruffo, R.; Fathi, R.; Kim, D. K. J.; Jung, Y. H.; Mari, C. M.; Kim, D. K. J. Impedance Analysis of Na_{0.44}MnO₂ Positive Electrode for Reversible Sodium Batteries in Organic Electrolyte. *Electrochim. Acta* **2013**, *108*, 575–582.
- (14) D'Arienzo, M.; Ruffo, R.; Scotti, R.; Morazzoni, F.; Mari, C. M.; Polizzi, S. Layered Na_{0.71}CoO₂: A Powerful Candidate for Viable and High Performance Na-Batteries. *Phys. Chem. Chem. Phys.* **2012**, *14* (17), 5945–5952.
- (15) Yabuuchi, N.; Kajiyama, M.; Iwatate, J.; Nishikawa, H.; Hitomi, S.; Okuyama, R.; Usui, R.; Yamada, Y.; Komaba, S. P₂-Type Na_x[Fe_{1/2}Mn_{1/2}]O₂ Made from Earth-Abundant Elements for Rechargeable Na Batteries. *Nat. Mater.* **2012**, *11* (6), 512–517.
- (16) Padhi, A. K.; Nanjundaswamy, K. S.; Goodenough, J. B. Phospho-olivines as Positive-Electrode Materials for Rechargeable Lithium Batteries. *J. Electrochem. Soc.* **1997**, *144* (4), 1188–1194.
- (17) Rechem, N.; Chotard, J.-N.; Dupont, L.; Djellab, K.; Armand, M.; Tarascon, J.-M. Ionothermal Synthesis of Sodium-Based Fluorophosphate Cathode Materials. *J. Electrochem. Soc.* **2009**, *156* (12), A993–A999.
- (18) Kundu, D.; Tripathi, R.; Popov, G.; Makahnouk, W. R. M.; Nazar, L. F. Synthesis, Structure, and Na-Ion Migration in Na₄NiP₂O₇F₂: A Prospective High Voltage Positive Electrode Material for the Na-Ion Battery. *Chem. Mater.* **2015**, *4906* (5), 5349.
- (19) Chen, C. Y.; Matsumoto, K.; Nohira, T.; Hagiwara, R.; Orikasa, Y.; Uchimoto, Y. Pyrophosphate Na₂FeP₂O₇ as a Low-Cost and High-Performance Positive Electrode Material for Sodium Secondary Batteries Utilizing an Inorganic Ionic Liquid. *J. Power Sources* **2014**, *246*, 783–787.
- (20) Chen, C.-Y.; Matsumoto, K.; Nohira, T.; Ding, C.; Yamamoto, T.; Hagiwara, R. Charge–discharge Behavior of a Na₂FeP₂O₇ Positive Electrode in an Ionic Liquid Electrolyte between 253 and 363K. *Electrochim. Acta* **2014**, *133*, 583–588.
- (21) Chung, S.; Yamada, Y.; Yamada, A. Na₂FeP₂O₇: A Safe Cathode for Rechargeable Sodium-Ion Batteries. *Chem. Mater.* **2013**, *25*, 3480.
- (22) Longoni, G.; Wang, J. E.; Jung, Y. H.; Kim, D. K.; Mari, C. M.; Ruffo, R. The Na₂FeP₂O₇-Carbon Nanotubes Composite as High Rate Cathode Material for Sodium Ion Batteries. *J. Power Sources* **2016**, *302*, 61–69.
- (23) Dahbi, M.; Yabuuchi, N.; Kubota, K.; Tokiwa, K.; Komaba, S. Negative Electrodes for Na-Ion Batteries. *Phys. Chem. Chem. Phys.* **2014**, *16*, 15007.
- (24) Klein, F.; Jache, B.; Bhide, A.; Adelhelm, P. Conversion Reactions for Sodium-Ion Batteries. *Phys. Chem. Chem. Phys.* **2013**, *15* (38), 15876–15887.
- (25) Chevrier, V.; Ceder, G. Challenges for Na-Ion Negative Electrodes. *J. Electrochem. Soc.* **2011**, *158* (9), A1011.
- (26) Zhang, S.; Li, W.; Tan, B.; Chou, S.; Li, Z.; Dou, S. One-Pot Synthesis of Ultra-Small Magnetite Nanoparticles on the Surface of Reduced Graphene Oxide Nanosheets as Anodes for Sodium-Ion Batteries. *J. Mater. Chem. A* **2015**, *3* (9), 4793–4798.
- (27) Kumar, P. R.; Jung, Y. H.; Bharathi, K. K.; Lim, C. H.; Kim, D. K. High Capacity and Low Cost Spinel Fe₃O₄ for the Na-Ion Battery Negative Electrode Materials. *Electrochim. Acta* **2014**, *146*, 503–510.
- (28) Wang, D.; Yu, Y.; He, H.; Wang, J.; Zhou, W.; Abruna, H. D. Template-Free Synthesis of Hollow-Structured Co₃O₄ Nanoparticles as High-Performance Anodes for Lithium-Ion Batteries. *ACS Nano* **2015**, *9*, 1775–1781.
- (29) Liu, Y.; Cheng, Z.; Sun, H.; Arandiyani, H.; Li, J.; Ahmad, M. Mesoporous Co₃O₄ sheets/3D Graphene Networks Nanohybrids for High-Performance Sodium-Ion Battery Anode. *J. Power Sources* **2015**, *273*, 878–884.
- (30) Su, Q.; Zhang, J.; Wu, Y.; Du, G. Revealing the Electrochemical Conversion Mechanism of Porous Co₃O₄ Nanoplates in Lithium Ion Battery by in Situ Transmission Electron Microscopy. *Nano Energy* **2014**, *9*, 264–272.
- (31) Yang, X.; Wang, C.; Yang, Y.; Zhang, Y.; Jia, X.; Chen, J.; Ji, X. Anatase TiO₂ Nanocubes for Fast and Durable Sodium Ion Battery Anodes. *J. Mater. Chem. A* **2015**, *3*, 8800–8807.
- (32) Wu, L.; Bresser, D.; Buchholz, D.; Giffin, G.; Castro, C. R.; Ochel, A.; Passerini, S. Unfolding the Mechanism of Sodium Insertion in Anatase TiO₂ Nanoparticles. *Adv. Energy Mater.* **2015**, *5*, 1–11.
- (33) Xiong, H.; Slater, M. D.; Balasubramanian, M.; Johnson, C. S.; Rajh, T. Amorphous TiO₂ Nanotube Anode for Rechargeable Sodium Ion Batteries. *J. Phys. Chem. Lett.* **2011**, *2*, 2560–2565.
- (34) Xu, Y.; Memarzadeh Lotfabad, E.; Wang, H.; Farbod, B.; Xu, Z.; Kohandehghan, A.; Mitlin, D. Nanocrystalline Anatase TiO₂: A New Anode Material for Rechargeable Sodium Ion Batteries. *Chem. Commun. (Cambridge, U. K.)* **2013**, *49* (79), 8973–8975.
- (35) Wu, L.; Buchholz, D.; Bresser, D.; Gomes Chagas, L.; Passerini, S. Anatase TiO₂ Nanoparticles for High Power Sodium-Ion Anodes. *J. Power Sources* **2014**, *251*, 379–385.
- (36) Kim, K.-T.; Ali, G.; Chung, K. Y.; Yoon, C. S.; Yashiro, H.; Sun, Y.-K.; Lu, J.; Amine, K.; Myung, S.-T. Anatase Titania Nanorods as an Intercalation Anode Material for Rechargeable Sodium Batteries. *Nano Lett.* **2014**, *14* (2), 416–422.
- (37) Dinh, C.-T.; Nguyen, T.-D.; Kleitz, F.; Do, T.-O. Shape-Controlled Synthesis of Highly Crystalline Titania Nanocrystals. *ACS Nano* **2009**, *3* (11), 3737–3743.
- (38) D'Arienzo, M.; Carbajo, J.; Bahamonde, A.; Crippa, M.; Polizzi, S.; Scotti, R.; Wahba, L.; Morazzoni, F. Photogenerated Defects in Shape-Controlled TiO₂ Anatase Nanocrystals: A Probe to Evaluate the Role of Crystal Facets in Photocatalytic Processes. *J. Am. Chem. Soc.* **2011**, *133* (44), 17652–17661.
- (39) Liu, G.; Yang, H. G.; Pan, J.; Yang, Y. Q.; Lu, G. Q. M.; Cheng, H. M. Titanium Dioxide Crystals with Tailored Facets. *Chem. Rev.* **2014**, *114* (19), 9559–9612.
- (40) Hummers, W. S.; Offeman, R. E. Preparation of Graphitic Oxide. *J. Am. Chem. Soc.* **1958**, *80* (1937), 1339.
- (41) Raju, M.; Van Duin, A. C. T.; Fichthorn, K. A. Mechanisms of Oriented Attachment of TiO₂ Nanocrystals in Vacuum and Humid Environments: Reactive Molecular Dynamics. *Nano Lett.* **2014**, *14* (4), 1836–1842.
- (42) Ge, Y.; Jiang, H.; Zhu, J.; Lu, Y.; Chen, C.; Hu, Y.; Qiu, Y.; Zhang, X. High Cyclability of Carbon-Coated TiO₂ Nanoparticles as Anode for Sodium-Ion Batteries. *Electrochim. Acta* **2015**, *157*, 142–148.
- (43) Perfonrranc, I.; Area, P.; Leaders, Q.; Teams, T. C.; Improvement, C.; Dmt, D. T. S.; Sepg, D.; Chen, C.; Wen, Y.; Hu, X.; Ji, X.; Yan, M.; Mai, L.; Hu, P.; Shan, B.; Huang, Y. Na(+) Intercalation Pseudocapacitance in Graphene-Coupled Titanium Oxide Enabling Ultra-Fast Sodium Storage and Long-Term Cycling. *Nat. Commun.* **2015**, *6*, 6929.
- (44) Li, N.; Zhou, G.; Fang, R.; Cheng, H.; Li, F.; Cheng, H. TiO₂/graphene Sandwich Paper as an Anisotropic Electrode for High Rate Lithium Ion Batteries. *Nanoscale* **2013**, *5* (17), 7780.
- (45) Tahir, M. N.; Oschmann, B.; Buchholz, D.; Dou, X.; Lieberwirth, I.; Panthöfer, M.; Tremel, W.; Zentel, R.; Passerini, S. Extraordinary Performance of Carbon-Coated Anatase TiO₂ as Sodium-Ion Anode. *Adv. Energy Mater.* **2016**, *6*, 1501489.
- (46) Wagemaker, M.; Borghols, W. J. H.; Mulder, F. M. Large Impact of Particle Size on Insertion Reactions. A Case for Anatase LiTi_xO₂. *J. Am. Chem. Soc.* **2007**, *129* (March), 4323–4327.
- (47) Augustyn, V.; Come, J.; Lowe, M. a.; Kim, J. W.; Taberna, P.-L.; Tolbert, S. H.; Abruna, H. D.; Simon, P.; Dunn, B. High-Rate Electrochemical Energy Storage through Li+ Intercalation Pseudocapacitance. *Nat. Mater.* **2013**, *12* (6), 518–522.

(48) Conway, B. E. E.; Birss, V.; Wojtowicz, J. The Role and Utilization of Pseudocapacitance for Energy Storage by Supercapacitors. *J. Power Sources* **1997**, *66* (1–2), 1–14.

(49) Chen, W.; Fan, Z.; Gu, L.; Bao, X.; Wang, C.; Miller, J. R.; Simon, P.; Simon, P.; Gogotsi, Y.; Zheng, J. P.; Cygan, P.; Jow, T.; Chang, J.; Tsai, W.; Lee, H. Y.; Kim, S. W.; Lee, H. Y.; Ma, S. B.; Nam, K. W.; Yoon, W. S.; Yang, X. Q.; Ahn, K. Y.; Oh, K. H.; Kim, K. B.; Xie, X.; Gao, L.; Raymundo-Pinero, E.; Khomenko, V.; Frackowiak, E.; Beguin, F.; Fan, Z.; Chen, J.; Zhang, B.; Liu, B.; Zhang, X.; Kuang, Y.; Zhang, H.; Cao, G.; Wang, Z.; Yang, Y.; Shi, Z.; Gu, Z.; Pang, S. C.; Anderson, M. A.; Chapman, T. W.; Chen, W.; Pan, X.; Willinger, M. G.; Su, D. S.; Bao, X.; Chen, W.; Pan, X.; Bao, X.; Pan, X.; Fan, Z.; Chen, W.; Ding, Y.; Luo, H.; Bao, X.; Chen, W.; Fan, Z.; Pan, X.; Bao, X.; Pan, X.; Bao, X.; Castillejos, E.; Debouttiere, P. J.; Roiban, L.; Solhy, A.; Martinez, V.; Kihn, Y.; Ersen, O.; Philippot, K.; Chaudret, B.; Serp, P.; Pennycook, S. J.; Eklund, P. C.; Holden, J. M.; Jishi, R. A.; Buciuman, F.; Patcas, F.; Craciun, R.; Zahn, D. R. T.; Bernard, M. C.; Goff, A. H. L.; Thi, B. V.; Torresi, S. C.; de Han, Y. F.; Chen, F.; Zhong, Z.; Ramesh, K.; Chen, L.; Widjaja, E.; Ugarte, D.; Chatelain, A.; Heer, W. A.; de Toupin, M.; Brousse, T.; Blanger, D.; Toupin, M.; Brousse, T.; Belanger, D.; Jeong, Y. U.; Manthiram, A.; Devaraj, S.; Munichandraiah, N.; Chmiola, J.; Yushin, G.; Gogotsi, Y.; Portet, C.; Simon, P.; Taberna, P. L.; Chmiola, J.; Largeot, C.; Taberna, P. L.; Simon, P.; Geogotsi, Y. Enhanced Capacitance of Manganese Oxide via Confinement inside Carbon Nanotubes. *Chem. Commun.* **2010**, *46* (22), 3905.

(50) Wang, J.; Polleux, J.; Lim, J.; Dunn, B. Pseudocapacitive Contributions to Electrochemical Energy Storage in TiO₂ (Anatase). *Nanoparticles* **2007**, *2*, 14925–14931.

(51) Dylla, A. G.; Henkelman, G.; Stevenson, K. J. Lithium Insertion in Nanostructured TiO₂ (B). *Acc. Chem. Res.* **2013**, *46* (5), 1104.

(52) Neugebauer, J.; Scheffler, M. Adsorbate-Substrate and Adsorbate-Adsorbate Interactions of Na and K Adlayers on Al(111). *Phys. Rev. B: Condens. Matter Mater. Phys.* **1992**, *46* (24), 16067–16080.

(53) Clark, S. J.; Segall, M. D.; Pickard, C. J.; Hasnip, P. J.; Probert, M. I. J.; Refson, K.; Payne, M. C. First Principles Methods Using CASTEP. *Z. Kristallogr. - Cryst. Mater.* **2005**, *220* (5–6), S67–S70.